Citation for final published version:

Lee, Juwon, Pak, Sangyeon, Lee, Young-Woo, Park, Youngsin, Jang, A-Rang, Hong, John, Cho, Yuljae, Hou, Bo , Lee, Sanghyo, Jeong, Hu Young, Shin, Hyeon Suk, Morris, Stephen M., Cha, SeungNam, Sohn, Jung Inn and Kim, Jong Min 2019. Direct epitaxial synthesis of selective two-dimensional lateral heterostructures. ACS Nano 13 (11) , pp. 13047-13055. 10.1021/acsnano.9b05722

Publishers page: http://dx.doi.org/10.1021/acsnano.9b05722

Direct Epitaxial Synthesis of Selective Two-Dimensional Lateral Heterostructures

Juwon Lee,[†,¶] *Sangyeon Pak,*[‡,¶] *Young-Woo Lee,*[§] *Youngsin Park,*[‖] *A-Rang Jang,*[†,#] *John Hong,*[†] *Yuljae Cho,*[†,▽] *Bo Hou,*[†,▽] *Sanghyo Lee,*[†,▽] *Hu Young Jeong,*[⊥] *Hyeon Suk Shin,*[○] *Stephen M. Morris,*[†] *SeungNam Cha,**[‡] *Jung Inn Sohn**[†,◆] *and Jong Min Kim*[▽]

[†] Department of Engineering Science, University of Oxford, Parks Road, Oxford OX1 3PJ, United Kingdom

[‡] Department of Physics, Sungkyunkwan University (SKKU) Suwon, Gyeonggi-do, 16419, Republic of Korea

[§] Department of Energy Systems, Soonchunhyang University, Asan, Chungcheongnam-do 31538, Republic of Korea

[‖] School of Natural Science, Ulsan National Institute of Science and Technology (UNIST), Ulsan, 44919, Republic of Korea

[#] Advanced Materials Division, Korea Research Institute of Chemical Technology (KRICT), Gajeong-ro 141, Daejeon, 34114, Republic of Korea

[▽] Electrical Engineering Division, Engineering Department, University of Cambridge, 9 JJ Thomson Avenue, Cambridge, CB3 0FA, United Kingdom

[⊥] UNIST Central Research Facilities (UCRF), Ulsan National Institute of Science and Technology (UNIST), 50 UNIST-gil, Ulsan, 44919, Republic of Korea

[○] Department of Chemistry, Ulsan National Institute of Science and Technology (UNIST),

50 UNIST-gil, Ulsan, 44919, Republic of Korea

[◆] Division of Physics and Semiconductor Science, Dongguk University-Seoul, Seoul 04620, Republic of Korea

Abstract

Two-dimensional (2D) heterostructured or alloyed monolayers composed of transition metal dichalcogenides (TMDCs) have recently emerged as promising materials with great potential for atomically thin electronic applications. However, fabrication of such artificial TMDC heterostructures with a sharp interface and a large crystal size still remains a challenge because of the difficulty in controlling various growth parameters simultaneously during the growth process. Here, a facile synthetic protocol designed for the production of the lateral TMDC heterostructured and alloyed monolayers is presented. A chemical vapor deposition approach combined with solution-processed precursor deposition makes it possible to accurately control the sequential introduction time and the supersaturation levels of the vaporized precursors, and thus reliably and exclusively produces selective and heterogeneous epitaxial growth of TMDC monolayer crystals. In addition, TMDC core/shell heterostructured (MoS_2/alloy, alloy/WS_2) or alloyed ($Mo_{1-x}W_xS_2$) monolayers are also easily obtained with precisely controlled growth parameters, such as sulfur introduction timing and growth temperature. These results represent a significant step toward the development of various 2D materials with interesting properties.

Keywords: one-pot CVD synthesis, 2D heterostructure, core-shell structure, $Mo_{1-x}W_xS_2$ alloy, growth parameters, supersaturation level

Two-dimensional atomic crystals, especially transition metal dichalcogenide (TMDC) monolayers, have drawn considerable attention due to their outstanding optical and electrical properties.[1-5] For example, TMDC monolayers undergo a transition from indirect to direct band gap when their thickness decreases to an atomically thin level,[3,6] which make them potential candidates for next-generation electronic and optoelectronic devices.[7-11] Moreover, recent developments in TMDC heterostructures have led to important advances in our understanding of their physical properties, including efficient exciton dissociation and ultrafast charge transfer.[12-15] Thus, many research groups have attempted to construct a variety of vertically stacked or laterally connected TMDC heterostructures in order to design atomically thin devices.[16-21] For TMDC vertical heterostructures, several epitaxial growth procedures have been reported,[22-24] however, most vertical TMDC heterostructures have been commonly employed by stacking different monolayers *via* physical transfer techniques.[25-27] Thus, the mismatch in the stacking angle between the monolayers[25] and the contaminants at the interface[26,27] are unavoidable.

Besides the vertical TMDC heterostructures, a few different strategies for the epitaxial growth of lateral TMDC heterostructures have recently been proposed on the basis of one-step[24,28-32] and two-step[12,33-38] chemical vapor deposition (CVD). Conceptually, two-step growth processes offer a more convenient approach to achieving controlled lateral heterostructures because each TMDC monolayer can be grown individually and sequentially. However, the edges of the core layer can easily be contaminated when it is exposed to ambient conditions between the first and second growth procedures, which can induce a large number of defects near the interface.[33] Consequently, these defect sites can play a significant role in nucleating precursors during the second growth step, thus resulting in a change in the growth kinetics. As a result, the two-step growth procedure of lateral TMDC heterostructures usually exhibits a composition transition region at the interface,[33] thicker outer-shell layers,[33,37] and/or the nucleation on the top of the inner core crystal.[12] In contrast, the one-step growth approach, which does not need to expose the edges of the core layer to ambient conditions, is much more favorable in creating lateral heterostructures with an atomically sharp interface. However, it is not easy to achieve the uniformity and reproducibility in the one-step synthesis because of the difficulty in controlling various precursors and growth parameters simultaneously. Thus, the one-step growth process can suffer from precursor mixing and hence produce undesirable alloyed structures at the interface.[39,40] Although some strategies, such as loading precursors in quartz boats facing down[29] and adding a metal catalyst to lower growth temperature,[24] have been suggested to avoid the interference of vaporized precursors, it still remains a challenge to synthesize lateral TMDC heterostructures with a clear interface and a large crystal size.

Here we demonstrate a facile one-pot CVD process for the compositionally-controlled monolayer growth of lateral core/shell (MoS_2/WS_2, MoS_2/alloy, and alloy/WS_2) heterostructures and $Mo_{1-x}W_xS_2$ alloys using a solution-processed precursor deposition technique so as to precisely control the sequential introduction timing and the supersaturation level of all the precursors. With this growth strategy, the metal oxide precursors can be vaporized separately or simultaneously in order to synthesize various types of heterostructures and alloys. Furthermore, the crystal size of the selectively controlled hetero-epitaxy of MoS_2/WS_2 monolayer is found to increase up to 160 um which is attributed to a thermodynamically controlled homogeneous nucleation of the core layer. The lateral heterostructures are clearly verified by Raman and photoluminescence (PL) spectra as well as transmission electron microscopy (TEM). Compared to the two-step growth, the MoS_2/WS_2 heterostructures grown by our one-step growth have a relatively clear interface. In addition, alloyed structures are intentionally obtained in the core or the shell regions of the lateral heterostructures, or over the whole region of the monolayer by controlling the relative vaporized amounts of precursors and the growth temperatures. Our growth strategies can be applied to other TMDC heterostructures and can provide a number of opportunities for the development of next-generation electronic and optoelectronic devices.

Results/Discussion

Figure 1a,b illustrates the growth procedure of the TMDC heterostructured or alloyed monolayers. As previously reported,[41] our solution-processed approach makes it possible to deposit an extremely small amount of transition metal oxide precursor onto the SiO_2 substrates to induce a low supersaturation level during the growth process, which in turn leads to the growth of large-sized and highly crystalline TMDC monolayers as well as the fast and complete consummation of the precursors within a short time frame. This is a crucial point for the successful production of lateral heterostructured or alloyed monolayer without any additional undesirable nucleation and growth. To apply this strategy to the growth of the TMDC monolayer heterostructures and alloys, a MoO_3 solution in ammonium hydroxide (NH_4OH) was spincoated or dropped onto the bottom SiO_2 substrate. The weight of the deposited MoO_3 film was found to be significantly small around ~0.01 mg. For the sufficient supply of tungsten source, tungsten trioxide (WO_3) precursors were scattered directly onto the growth substrate, using a solution made from dissolving WO_3 and sodium cholate together in NH_4OH, because the vapor concentration of the WO_3 powder is much lower than that of MoO_3 even at a high temperature over 950 °C. The heavy weight of the sodium cholate could make it possible to deposit WO_3 in the form of particles, and its carbon ring structure plays an important role in nucleating TMDC monolayers rather easily.[42] After the deposition of the precursor, the substrates that have a MoO_3 film and WO_3

particles were loaded on the bottom and the top of the crucible in a furnace, respectively, as shown in Figure 1b.

Our one-step CVD growth procedure at atmospheric pressure employs three main parameters to synthesize the various TMDC monolayer heterostructures and alloys by decoupling and coupling the MoS_2 and the WS_2 growth processes: (1) the sulfur vaporization temperature, (2) the subsequent growth temperature, and (3) the relative supersaturation level of MoO_3 and WO_3 during the synthesis. The four types of monolayer structures laterally grown using our approach are summarized in Figure 1c: MoS_2/WS_2 heterostructures (Type A), MoS_2/alloy heterostructures (Type B), alloy/WS_2 heterostructures (Type C), and alloy monolayer structures (Type D). The effect of parameters on the grow behavior were carefully studied and compared as shown in Figure S1. From these results, the role of each parameter can be determined as follows, which will be also explained in further detail later in this report:

(1) The sulfur vapor introduction temperature determines whether the core structure will be grown as a single MoS_2 monolayer or a $Mo_{1-x}W_xS_2$ alloy. At a low temperature (~680 °C), a single MoS_2 monolayer is formed inside (Type A & B) because the vaporization and sulfurization of WO_3 rarely occurs at such comparatively low temperature due to the relatively high vaporization temperature of WO_3. However, if the sulfur vaporization begins at a high temperature (~840 °C), then MoO_3 and WO_3 will be vaporized and reacted with the vapor-phase sulfur simultaneously to yield an alloy-type monolayer in the core (Type C & D);

(2) The subsequent growth for lateral epitaxial growth continuously over the existing core crystal edges is mainly implemented at a relatively high temperature (~950 °C) so as to facilitate the vaporization of WO_3 from the middle to the final growth phase (Type B, C & D). It is worth noting that the final growth temperature was kept as low as possible when synthesizing a clear MoS_2/WS_2

heterostructure (Type A). If the final growth temperature is increased, a narrow MoS_2/WS_2 alloy band is frequently found at the interface of the heterostructure because MoO_3 can be vaporized violently at a high temperature and coexist with WO_3 precursors in the vapor phases until it is completely consumed (Structure no. 5 & 6 in Figure S1, and Figure S2);

(3) The supersaturation level associated with the vapor concentration and pressure of precursors is the determining factor in producing the desired heterostructure. The low supersaturation level of MoO_3 was used to grow the second WS_2 material at the edge of the first core crystal by avoiding the undesired alloyed formation at the interface or in the shell layer of the heterostructure (Type A & C). The high supersaturation level of WO_3 was usually employed to promote the formation of alloy in the shell layer by maintaining a high vapor concentration of WO_3 (Type B & C). Also, note that the low supersaturation level of WO_3 was used to grow in-plane lateral MoS_2/WS_2 heterostructures, whereas vertical heterostructures were frequently found together with lateral heterostructures when applying a high supersaturation level of WO_3 (Structure no. 1 in Figure S1, and Figure S3). Finally, it has shown that the composition of the $Mo_{1-x}W_xS_2$ alloy monolayers (Type D) can be easily controlled by adjusting the supersaturation level of MoO_3 and WO_3.

Figure 2a shows that large MoS_2/WS_2 lateral heterostructured crystals were grown on the SiO_2 substrates. It was confirmed that the MoS_2 monolayer was grown first at a relatively low temperature and then the WS_2 monolayers started to grow laterally from the edge of the MoS_2 monolayers. The shape of the synthesized WS_2 monolayers tended to follow that of the MoS_2 monolayer, which is very similarly to that found on the other parts of the growth substrate (Figure S4). The sizes of the heterostructures were much larger than that of previously reported heterostructures, and the size of the triangular crystals reached up to 160 μm (Figure 2b). The MoS_2 and WS_2 regions could be clearly discerned in a single triangular domain due to the optical contrast difference between them (Figure 2c). The MoS_2/WS_2 heterostructures were further examined by Raman and PL spectra (Figure 2d,e). The Raman and PL spectra of the MoS_2 and WS_2 monolayers were obtained from the points marked as red and green dots in Figure 2c, respectively. The 2LA(M) resonance peak and the A'_1 peak of the WS_2 monolayer were clearly seen at around 349 cm^{-1} and 417 cm^{-1} in the shell region, respectively, while the MoS_2 monolayer in the core region exhibited two characteristic Raman peaks at around 382 cm^{-1} and 401 cm^{-1}, corresponding to the E' mode and the A'_1 mode, respectively.[43,44] Similarly, two distinctive peaks at 1.83 eV and 1.97 eV were found in the PL spectra, which corresponds to the emission from the MoS_2 and WS_2 monolayers, respectively.

To further verify the spatial distributions of the lateral heterostructures, the Raman and PL mapping images (Figure 2f-i) were taken from the crystal in Figure 2b. These mapping images clearly show that the MoS_2 monolayer in the core region interconnected seamless with the WS_2 domain in the outer region. The transition graph of the PL spectra collected at the interface of the heterostructure (marked as a white dotted line in Figure 2c) also demonstrates that the MoS_2 and WS_2 regions were clearly separated, and the intermediate state peak, which might have originated from alloyed structures at the interface, was not observed at the interface as shown in Figure 2j. The formation of the clear interface was further confirmed using an atomic resolution Z-contrast scanning transmission electron microscope (STEM) image (Figure 2k). In addition, an in-plane MoS_2/WS_2 device was fabricated to investigate the electrical properties of the heterostructures (Figure 2l). The forward bias current is about three orders of magnitude higher than the reverse current, which means that the heterostructure device showed a good rectifying characteristic.

The clear interface and the large sizes of the heterostructures we obtained, especially for Type A in Figure 1c, can be explained by considering in more depth our growth strategy. In our growth procedure, an extremely small amount of MoO_3 was deposited using a solution-processed precursor deposition technique. As a result, the supersaturation level of MoO_3 becomes rather low during the growth of the first inner MoS_2 crystal, and thus the nucleation density decreased dramatically, which in turn increases the size of the synthesized crystal as shown in our previous report.[41] In addition, the interference from vaporized MoO_3 molecules was dramatically suppressed during the successive growth of the WS_2 monolayer because the growth of the MoS_2 monolayers can usually be completed in a short timescale (< 5 minutes) at the early stages of the growth process due to the extremely small amount of the MoO_3 precursor (~0.01 mg), resulting in the MoS_2/WS_2 lateral heterostructure with a sharp one-dimensional interface.

To further provide interesting insights into our direct one-step growth process in the formation of high-quality in-plane heterostructures, two-step growth processes for lateral MoS_2/WS_2 heterostructures was also conducted (Figure S5). The growth of the MoS_2 monolayer was followed by the growth of the WS_2 monolayer sequentially under similar synthetic conditions. Interestingly, unlike a one-step growth, the intermediate state peak was clearly observed in the PL measurement in the crystal grown using the two-step growth procedure. The PL mapping and spectra show that the intermediate peak was located at 1.91 eV at the interface between the MoS_2 and the WS_2 monolayers. This compositional transition region at the interface might be attributed to defect sites generated at the edge of the inner layer when the layer was exposed to the ambient environment in preparation for the second growth. As a result, a large number of defect sites could result in a change in the nucleation and lateral growth kinetics for the subsequent epitaxial heterostructure growth process.[33] The possibility of the presence of MoO_3 precursors during the second WS_2 growth was excluded because different quartz tubes were used for each of the MoS_2

and WS_2 monolayer growth. In addition, the diffusion-mediated synthesis at a relatively high temperature might be another factor causing the formation of the transition region.[36]

As shown in Figure 1c, the composition of the core and the shell layers in the heterostructures can be adjusted by controlling the growth parameters. For the MoS_2/alloy lateral heterostructure, the final growth temperature and the amount of the deposited MoO_3 were increased to 950 °C and 0.1 mg, respectively, to keep the vapor concentration of MoO_3 high throughout until the outer shell layer had formed. As a result, a $Mo_{1-x}W_xS_2$ alloyed monolayer was formed in the outer shell (Figure 3a,b). Although the optical contrast is weaker than that of the MoS_2/WS_2 heterostructured monolayer, the alloyed region in the shell could be distinguished from the MoS_2 monolayer area in the core. The Raman spectra of the MoS_2/alloy heterostructure show that the corresponding peaks of the MoS_2 and the WS_2 monolayers were observed simultaneously at the outer shell, indicating the formation of an alloyed layer, while only MoS_2 monolayer peaks were found in the core region (Figure 3c). It is further found that the E' and the A'_1 peaks peaks of MoS_2 and the 2LA(M) peak of WS_2 in the alloyed outer shell became much weaker and broader than those typically observed for WS_2 monolayers. The PL spectra in Figure 3d also demonstrate that the emission energy level of the outer shell (1.87 eV) was found to be within the range between those of the MoS_2 and the WS_2 monolayers, revealing the formation of an alloy heterostructures. The uniformity of the core and the outer shell was confirmed by the Raman and PL mapping images (Figure 3e). The composition ratio of the outer shell was calculated using the equation,

$$E_{\mathrm{Mo_{1-x}W_xS_2}} = (1-x)E_{\mathrm{MoS_2}} + xE_{\mathrm{WS_2}} - bx(1-x) \qquad (1)$$

where $E_{\mathrm{Mo_{1-x}W_xS_2}}$, $E_{\mathrm{MoS_2}}$, and $E_{\mathrm{WS_2}}$ are the band gaps of the alloy, MoS_2, and WS_2 monolayer, respectively, and b is the bowing parameter.[45] In this case, the composition ratio is found to be $x = 0.3$, which shows that $Mo_{0.7}W_{0.3}S_2$ monolayer was formed in the shell layer.

Using the lateral epitaxial growth strategy, we have also designed growth parameters so as to synthesize an in-plane heterostructure consisting of an alloyed structure in the core and a WS_2 only monolayer in the outer shell as shown in Figure 4a,b. To first form an alloyed layer as the core of the lateral heterostructure, the sulfur vaporization started at a much higher temperature (840 °C) than that for the growth of the MoS_2/WS_2 heterostructure in Figure 2. In addition, the relatively large amount of WO_3 was loaded, while the small amount of MoO_3, similar to that for the MoS_2/WS_2 heterostructure growth process, was loaded in order to avoid any unwanted alloy reaction during the subsequent epitaxial growth of the outer WS_2 shell. The Raman spectrum showed that both the MoS_2 and the WS_2 monolayer peaks were found in the core region, and only the WS_2 monolayer peaks were observed in the shell area (Figure 4c), confirming the alloy/WS_2 lateral heterostructures were formed. It was also found that the PL spectrum of the alloyed structure in the core region was slightly red-shifted and broader, compared to that of the WS_2 monolayer in the shell region (Figure 4d). Here, the composition ratio was found to be $x = 0.9$. The Raman and PL mapping images clearly show that the alloy core region and the pure WS_2 shell region are separated (Figure 4e). Note that the composition of the alloy core region can be controlled when the supersaturation level of WO_3 is relatively lowered by adjusting the ratio of the amount of the MoO_3 and WO_3 (Figure S6). In addition, the STEM image (Figure S7) clearly shows distinctively clear the $Mo_{1-x}W_xS_2$ and WS_2 regions in the alloy-WS_2 heterostructure, indicating that the dramatic suppression of the MoO_3 precursor led to avoid any unwanted alloy reaction during the subsequent epitaxial growth of the outer WS_2 shell.

Finally, we demonstrated the possibility that well-organized alloyed monolayers could be produced by controlling the relative amount of MoO_3 and WO_3 and using a high sulfur vaporization temperature (~840 °C) and a high growth temperature (950 °C). Figure 5a shows the resulting $Mo_{1-x}W_xS_2$ alloy monolayer grown laterally on the SiO_2 substrate. The PL intensity and position mapping images in Figure 5b,c show that the chemical composition and structural characteristics are uniform over the monolayer crystal. The emission energy of the alloy monolayer was 1.90 eV, which is located almost at the center of those of the MoS_2 and the WS_2 monolayers. The individual Raman spectra collected from the different areas of the alloy structure in Figure 5a exhibited almost the same profile, indicating the uniformity of the alloyed monolayer structure (Figure 5d). In addition, there was no significant difference in the position and the intensity of PL spectrum (Figure 5e). The composition ratio of the alloy monolayer could be easily controlled by adjusting the relative ratio of the amount of the MoO_3 and WO_3, thus we could obtain alloy monolayers with controlled energy band gaps. The emission energy level was close to that of the MoS_2 monolayer when the relative amount of MoO_3 was large, and vice-versa (Figure 5f).

To investigate the excitonic properties of the $Mo_{1-x}W_xS_2$ alloy monolayer, the temperature-dependent PL measurements were carried out as shown in Figure 5g. At a temperature below 100 K, an additional emission peak at around 1.85 eV was noticeable, and this peak became strongly dominant at 4.4 K. As the position of the newly emerged peak was stable with various excitation power at 4.4 K and has a broad width, it was thought to be related to bound excitons, compared to free excitons located at a high energy level (Figure S8). This shows that there are a number of binding sites in the alloy monolayer because Mo and W atoms are randomly distributed and mixed together in the crystal, which may be the reason why the bound excitons were observed only at low temperatures. The Varshni equation,[46] $E_g(T) = E_g(0) - aT^2/(T + b)$, was used to describe the band gap reduction with temperature. The transition of the free exciton was in good agreement with the Varshni equation, with $E_g(0) = 1.943$ eV, $a = 4.1 \times 10^{-4}$ eV K^{-1}, and $b = 406$ K. However, the bound exciton exhibited a transition point at around 75 K. When the temperature increases above 4.4 K, the bound excitons can be thermally activated into the free state, thus the peak position is expected to be red-shifted. With a further increase of the temperature above 75 K, non-radiative decay can have a significant effect on the emission process and decrease the decay time. These carriers recombine before they reach the lowest energy level in the conduction band, which leads to a blue shift in the PL spectrum.[47] A dramatic increase of the full-width-half-maximum (FWHM) of the bound exciton at around 75 K was also observed, while it remained almost constant below 50 K. In contrast, the FWHM of the free exciton increased gradually with increasing temperature, similar to those of typical semiconductors. These findings indicate that the emission behavior of the alloy monolayer structure can be significantly affected by the inhomogeneities and the binding sites in the crystal.

Conclusion

In conclusion, large-sized lateral MoS_2/WS_2 heterostructured monolayers with a clear interface have been synthesized directly on SiO_2 substrates by controlling the amount of metal oxide precursors *via* a solution-processed precursor deposition technique. The extremely small amount of the precursor can reduce its effect during the growth of the shell layer, which makes it possible to continuously synthesize lateral MoS_2/WS_2 heterostructures with atomically clear heterogenous junction and a large crystal size up to 160 μm. In addition, lateral MoS_2/alloy and alloy/WS_2 heterostructures have been readily obtained by controlling growth parameters such as the temperature at which sulfur is introduced, the final growth temperature, and the supersaturation level of MoO_3 and WO_3. Finally, uniform $Mo_{1-x}W_xS_2$ alloy monolayer could also be synthesized with a moderate amount of precursors, and bound excitons have been found to emerge at a low temperature and become strongly dominant below 50 K because of the trapped sites that arise from the random mixture of different transition metals. The current findings can be of significant importance in the utilization of TMDC heterostructure for various innovations in electronic and optoelectronic devices.

Methods/Experimental

Preparation of precursor solutions: a MoO_3 solution with various concentration (0.1-100 mg/ml) was prepared by adding MoO_3 powder (Sigma Aldrich) into NH_4OH (28-30% solution, Sigma Aldrich) in a small vial. The solution was sonicated and stirred over 10 minutes. A WO_3 solution was also prepared similarly to the MoO_3 solution. However, the WO_3 solution was sonicated and stirred at 90 °C for more than 2 hours because a WO_3 powder rarely dissolve in NH_4OH at room temperature. In addition, sodium cholate was additionally added to the WO_3 solution.

CVD growth of heterostructures and alloys: silicon substrates with 300 nm of SiO_2 were used as substrates. A MoO_3 film was spin coated onto a substrate with a drop of MoO_3 solution at 3000 rpm for 1 minutes, and then annealed at 300 °C for 10 minutes. WO_3 particles were scattered onto another substrate using a WO_3 solution. The substrates containing a MoS_2 film and WO_3 particles were put on the bottom and top of a crucible in a furnace, respectively. Sulfur powder (Sigma Aldrich) in another crucible was placed upstream at the edge of the tube. To synthesize various type of heterostructures and alloys, sulfur introduction and growth temperature were controlled according to the conditions as mentioned in Figure 1c, and the growth time was kept for 5 minutes.

Raman and PL measurement: Raman and PL measurement: the room temperature Raman and PL measurement were conducted in a Jobin Yvon LabRam Aramis Raman spectroscopy using a 532 nm laser with a power of ~20 μW and a spot size of 1.09 μm^2. For the low-temperature PL measurement, the sample was mounted in a continuous-flow helium cryostat, and the temperature was controlled from 4.2 K to room temperature.

Device fabrication and measurement: the MoS_2/WS_2 heterostructure device were fabricated by a standard e-beam lithography and lift-off process. The Ti/Au electrodes were deposited by thermal evaporation. Electrical measurements were performed at room temperature after thermal annealing at around 200 °C for more than 2 hours in vacuum. Finally, characterization of the electrical properties was carried out using a Keithley 4200-SCS Parameter Analyzer and a Cascade Microtech probe station.

Supporting Information

Detailed schematic illustration of the four growth parameters, MoS_2/alloy/WS_2 heterostructures, vertical MoS_2/WS_2 heterostructures, lateral MoS_2/WS_2 heterostructures, MoS_2/WS_2 heterostructures grown by two-step process, and light intensity dependent PL spectrum of the $Mo_{1-x}W_xS_2$ alloyed monolayer

Corresponding Authors

*Email: chasn@skku.edu

*Email: junginn.sohn@dongguk.edu

Author Contributions

¶J. L. & S. P. contributed equally to this work. J.L., S.P., J.I.S., S.C. and J.M.K. planned the project and wrote the manuscript. J.L. and S.P. grew the material and designed the device and performed the experiment and analyzed the data. Y.-W.L. investigated the structural and chemical characteristics of the material. Y.P. conducted low-temperature PL measurement. H.Y.J. and H.S.S conducted TEM measurement. A.-R.J, J.H., Y.C., B.H., S.L. and S.M.M. contributed to the interpretation of the data and commented on the manuscript.

Acknowledgement

The research leading to these results has received funding from the European Research Council under the European Union's Seventh Framework Programme (FP/2007-2013) / ERC Grant Agreement no. 340538. In addition, SMM would also like to thank The Royal Society for financial support. This research was supported by the National Research Foundation of Korea (NRF) grant funded by the Korea government (MSIT) (2019R1A2C1007883, 2019R1A2C1005930, 2019M1A2A2065616), and by Basic Science Research Program through the National Research Foundation of Korea (NRF) funded by the Ministry of Education (2016R1A6A1A03012877).

References

(1) Radisavljevic, B.; Radenovic, A.; Brivio, J.; Giacometti, V.; Kis, A., Single-Layer MoS2 Transistors. *Nat. Nanotechnol.* **2011,** *6*, 147-150.

(2) Radisavljevic, B.; Kis, A., Mobility Engineering and a Metal–Insulator Transition in Monolayer MoS_2. *Nat. Mater.* **2013,** *12*, 815-820.

(3) Mak, K. F.; Lee, C.; Hone, J.; Shan, J.; Heinz, T. F., Atomically Thin MoS2: a New Direct-Gap Semiconductor. *Phys. Rev. Lett.* **2010,** *105*, 136805.

(4) Mak, K.; He, K.; Lee, C.; Lee, G.; Hone, J.; Heinz, T. F.; Shan, J., Tightly Bound Trions in Monolayer MoS_2. *Nat. Mater.* **2012,** *12*, 207-211.

(5) Splendiani, A.; Sun, L.; Zhang, Y.; Li, T.; Kim, J.; Chim, C.-Y. Y.; Galli, G.; Wang, F., Emerging Photoluminescence in Monolayer MoS_2. *Nano Lett.* **2010,** *10*, 1271-1275.

(6) Zhang, Y.; Chang, T.-R.; Zhou, B.; Cui, Y.-T.; Yan, H.; Liu, Z.; Schmitt, F.; Lee, J.; Moore, R.; Chen, Y.; Lin, H.; Jeng, H. -T.; Mo, S. -K.; Hussain, Z.; Bansil, A.; Shen, Z. -X., Direct Observation of the Transition from Indirect to Direct Bandgap in Atomically Thin Epitaxial $MoSe_2$. *Nat. Nanotechnol.* **2014,** *9*, 111-115.

(7) Yoon, J.; Park, W.; Bae, G. Y.; Kim, Y.; Jang, H.; Hyun, Y.; Lim, S.; Kahng, Y.; Hong, W. K.; Lee, B.; Ko, H. C., Highly Flexible and Transparent Multilayer MoS_2 Transistors with Graphene Electrodes. *Small* **2013,** *9*, 3295-3300.

(8) Pu, J.; Yomogida, Y.; Liu, K.-K.; Li, L.-J.; Iwasa, Y.; Takenobu, T., Highly Flexible MoS_2 Thin-Film Transistors with Ion Gel Dielectrics. *Nano Lett.* **2012,** *12*, 4013-4017.

(9) Pu, J.; Li, L.-J.; Takenobu, T., Flexible and Stretchable Thin-Film Transistors based on Molybdenum Disulphide. *Phys. Chem. Chem. Phys.* **2014,** *16*, 14996-15006.

(10) Pak, S.; Cho, Y.; Hong, J.; Lee, J.; Lee, S.; Hou, B.; An, G. H.; Lee, Y. W.; Jang, J. E.; Im, H.; Morris, S. M.; Sohn, J. I.; Cha, S.; Kim, J. M., Consecutive Junction-Induced Efficient Charge Separation Mechanisms for High-Performance MoS2/Quantum Dot Phototransistors. *ACS Appl. Mater. Interfaces* **2018,** *10*, 38264-38271.

(11) Pak, S.; Jang, A. R.; Lee, J.; Hong, J.; Giraud, P.; Lee, S.; Cho, Y.; An, G. H.; Lee, Y. W.; Shin, H. S.; Morris, S. M.; Cha, S.; Sohn, J. I.; Kim, J. M., Surface Functionalization-Induced Photoresponse Characteristics of Monolayer MoS2 for Fast Flexible Photodetectors. *Nanoscale* **2019,** *11*, 4726-4734.

(12) Heo, H.; Sung, J.; Jin, G.; Ahn, J. H.; Kim, K.; Lee, M. J.; Cha, S.; Choi, H.; Jo, M. H., Rotation-Misfit-Free Heteroepitaxial Stacking and Stitching Growth of Hexagonal Transition-Metal Dichalcogenide Monolayers by Nucleation Kinetics Controls. *Adv. Mater.* **2015,** *27*, 3803-3810.

(13) Shi, J.; Tong, R.; Zhou, X.; Gong, Y.; Zhang, Z.; Ji, Q.; Zhang, Y.; Fang, Q.; Gu, L.; Wang, X.; Liu, Z.; Zhang, Y., Temperature-Mediated Selective Growth of MoS2/WS2 and WS2/MoS2 Vertical Stacks on Au Foils for Direct Photocatalytic Applications. *Adv. Mater.* **2016,** *28*, 10664-10672.

(14) Chen, H.; Wen, X.; Zhang, J.; Wu, T.; Gong, Y.; Zhang, X.; Yuan, J.; Yi, C.; Lou, J.; Ajayan, P. M.; Zhuang, W.; Zhang, G.; Zheng, G., Ultrafast Formation of Interlayer Hot Excitons in Atomically Thin MoS2/WS2 Heterostructures. *Nat. Commun.* **2016,** *7*, 12512.

(15) Pak, S.; Lee, J.; Lee, Y.-W.; Jang, A.-R.; Ahn, S.; Ma, K. Y.; Cho, Y.; Hong, J.; Lee, S.; Jeong, H. Y.; Im, H.; Shin, H. S.; Morris, S. M.; Cha, S.; Sohn, J. I.; Kim, J. M., Strain-Mediated Interlayer Coupling Effects on the Excitonic Behaviors in an Epitaxially Grown MoS2/WS2 van der Waals Heterobilayer. *Nano Lett.* **2017,** *17*, 5634-5640.

(16) Cheng, R.; Li, D.; Zhou, H.; Wang, C.; Yin, A.; Jiang, S.; Liu, Y.; Chen, Y.; Huang, Y.; Duan, X., Electroluminescence and Photocurrent Generation from Atomically Sharp WSe2/MoS2 Heterojunction *p–n* Diodes. *Nano Lett.* **2014,** *14*, 5590-5597.

(17) Lee, C.-H.; Lee, G.-H.; van der Zande, A. M.; Chen, W.; Li, Y.; Han, M.; Cui, X.; Arefe, G.; Nuckolls, C.; Heinz, T. F.; Guo, J.; Hone, J.; Kim, P., Atomically Thin *p–n* Junctions with van der Waals Heterointerfaces. *Nat. Nanotechnol.* **2014,** *9*, 676-681.

(18) Furchi, M. M.; Pospischil, A.; Libisch, F.; Burgdörfer, J.; Mueller, T., Photovoltaic Effect in an Electrically Tunable van der Waals Heterojunction. *Nano Lett.* **2014,** *14*, 4785-4791.

(19) Choudhary, N.; Park, J.; Hwang, J.; Chung, H.-S.; Dumas, K. H.; Khondaker, S. I.; Choi, W.; Jung, Y., Centimeter Scale Patterned Growth of Vertically Stacked Few Layer Only 2D MoS_2/WS_2 van der Waals Heterostructure. *Sci. Rep.* **2016,** *6*, 25456.

(20) Xue, Y.; Zhang, Y.; Liu, Y.; Liu, H.; Song, J.; Sophia, J.; Liu, J.; Xu, Z.; Xu, Q.; Wang, Z.; Zheng, J.; Liu, Y.; Li, S.; Bao, Q., Scalable Production of a Few-Layer MoS_2/WS_2 Vertical Heterojunction Array and Its Application for Photodetectors. *ACS Nano* **2015,** *10*, 573-580.

(21) Woods, J. M.; Jung, Y.; Xie, Y.; Liu, W.; Liu, Y.; Wang, H.; Cha, J. J., One-Step Synthesis of MoS_2/WS_2 Layered Heterostructures and Catalytic Activity of Defective Transition Metal Dichalcogenide Films. *ACS Nano* **2016,** *10*, 2004-2009.

(22) Yu, Y.; Hu, S.; Su, L.; Huang, L.; Liu, Y.; Jin, Z.; Purezky, A. A.; Geohegan, D. B.; Kim, K.; Zhang, Y.; Cao, L., Equally Efficient Interlayer Exciton Relaxation and Improved Absorption in Epitaxial and Nonepitaxial MoS_2/WS_2 Heterostructures. *Nano Lett.* **2015,** *15*, 486-491.

(23) Zhang, Q.; Xiao, X.; Zhao, R.; Lv, D.; Xu, G.; Lu, Z.; Sun, L.; Lin, S.; Gao, X.; Zhou, J.; Jin, C.; Ding, F.; Jiao, L., Two-Dimensional Layered Heterostructures Synthesized from Core–Shell Nanowires. *Angew. Chem. Int. Ed.* **2015,** *54*, 8957-8960.

(24) Gong, Y.; Lin, J.; Wang, X.; Shi, G.; Lei, S.; Lin, Z.; Zou, X.; Ye, G.; Vajtai, R.; Yakobson, B. I.; Terrones, H.; Tay, B. K.; Lou, J.; Pantelides, S. T.; Liu, Z.; Zhou, W.; Ajayan, P. M., Vertical and In-Plane Heterostructures from WS2/MoS2 Monolayers. *Nat. Mater.* **2014,** *13*, 1135-1142.

(25) Nayak, P. K.; Horbatenko, Y.; Ahn, S.; Kim, G.; Lee, J.-U.; Ma, K. Y.; Jang, A. R.; Lim, H.; Kim, D.; Ryu, S.; Cheong, H.; Park, N.; Shin, H. S., Probing Evolution of Twist-Angle-Dependent Interlayer Excitons in $MoSe_2$/WSe_2 van der Waals Heterostructures. *ACS Nano* **2017,** *11*, 4041-4050.

(26) Zhu, X.; Monahan, N. R.; Gong, Z.; Zhu, H.; Williams, K. W.; Nelson, C. A., Charge Transfer Excitons at van der Waals Interfaces. *J. Am. Chem. Soc.* **2015,** *137*, 8313-8320.

(27) Li, H.; Wu, J.; Huang, X.; Yin, Z.; Liu, J.; Zhang, H., A Universal, Rapid Method for Clean Transfer of Nanostructures onto Various Substrates. *ACS Nano* **2014,** *8*, 6563-6570.

(28) Zhang, X.-Q.; Lin, C.-H.; Tseng, Y.-W.; Huang, K.-H.; Lee, Y.-H., Synthesis of Lateral Heterostructures of Semiconducting Atomic Layers. *Nano Lett.* **2015,** *15*, 410-415.

(29) Chen, K.; Wan, X.; Xie, W.; Wen, J.; Kang, Z.; Zeng, X.; Chen, H.; Xu, J., Lateral Built-In Potential of Monolayer MoS_2-WS_2 In-Plane Heterostructures by a Shortcut Growth Strategy. *Adv. Mater.* **2015,** *27*, 6431-6437.

(30) Sahoo, P. K.; Memaran, S.; Xin, Y.; Balicas, L.; Gutierrez, H. R., One-Pot Growth of Two-Dimensional Lateral Heterostructures *via* Sequential Edge-Epitaxy. *Nature* **2018,** *553*, 63-67.

(31) Zhang, Z.; Chen, P.; Duan, X.; Zang, K.; Luo, J.; Duan, X., Robust Epitaxial Growth of Two-Dimensional Heterostructures, Multiheterostructures, and Superlattices. *Science* **2017,** *357*, 788-792.

(32) Chiu, M. H.; Tang, H. L.; Tseng, C. C.; Han, Y.; Aljarb, A.; Huang, J. K.; Wan, Y.; Fu, J. H.; Zhang, X. X.; Chang, W. H.; Muller, D. A.; Takenobu, T.; Tung, V.; Li, L. -J., Metal-Guided

Selective Growth of 2D Materials: Demonstration of a Bottom-Up CMOS Inverter. *Adv. Mater.* **2019,** *31*, 1900861.

(33) Chen, K.; Wan, X.; Wen, J.; Xie, W.; Kang, Z.; Zeng, X.; Chen, H.; Xu, J.-B. B., Electronic Properties of MoS_2-WS_2 Heterostructures Synthesized with Two-Step Lateral Epitaxial Strategy. *ACS Nano* **2015,** *9*, 9868-9876.

(34) Yoo, Y.; Degregorio, Z. P.; Johns, J. E., Seed Crystal Homogeneity Controls Lateral and Vertical Heteroepitaxy of Monolayer MoS_2 and WS_2. *J. Am. Chem. Soc.* **2015,** *137*, 14281-14287.

(35) Ling, X.; Lin, Y.; Ma, Q.; Wang, Z.; Song, Y.; Yu, L.; Huang, S.; Fang, W.; Zhang, X.; Hsu, A. L.; Bie, Y.; Lee, Y. -H.; Zhu, Y.; Wu, L.; Li, J.; Jarillo-Herrero, P.; Dresselhaus, M.; Palacios, T.; Kong, J., Parallel Stitching of 2D Materials. *Adv. Mater.* **2016,** *28*, 2322-2329.

(36) Bogaert, K.; Liu, S.; Chesin, J.; Titow, D.; Gradečak, S.; Garaj, S., Diffusion-Mediated Synthesis of MoS2/WS2 Lateral Heterostructures. *Nano Lett.* **2016,** *16*, 5129-5134.

(37) Gong, Y.; Lei, S.; Ye, G.; Li, B.; He, Y.; Keyshar, K.; Zhang, X.; Wang, Q.; Lou, J.; Liu, Z.; Vajtai, R.; Zhou, W.; Ajayan, P. M., Two-Step Growth of Two-Dimensional WSe2/MoSe2 Heterostructures. *Nano Lett.* **2015,** *15*, 6135-6141.

(38) Li, M.-Y.; Shi, Y.; Cheng, C.-C.; Lu, L.-S.; Lin, Y.-C.; Tang, H.-L.; Tsai, M.-L.; Chu, C.-W.; Wei, K.-H.; He, J.-H.; Chang, W. -H.; Suenaga, K.; Li, L. -J., Epitaxial Growth of a Monolayer WSe2-MoS2 Lateral *p-n* Junction with an Atomically Sharp Interface. *Science* **2015,** *349*, 524-528.

(39) Huang, C.; Wu, S.; Sanchez, A. M.; Peters, J. J. P.; Beanland, R.; Ross, J. S.; Rivera, P.; Yao, W.; Cobden, D. H.; Xu, X., Lateral Heterojunctions within Monolayer $MoSe_2$-WSe_2 Semiconductors. *Nat. Mater.* **2014,** *13*, 1096-1101.

(40) Duan, X.; Wang, C.; Shaw, J. C.; Cheng, R.; Chen, Y.; Li, H.; Wu, X.; Tang, Y.; Zhang, Q.; Pan, A.; Jiang, J.; Yu, R.; Huang, Y.; Duan, X., Lateral Epitaxial Growth of Two-Dimensional Layered Semiconductor Heterojunctions. *Nat. Nanotechnol.* **2014,** *9*, 1024-1030.

(41) Lee, J.; Pak, S.; Giraud, P.; Lee, Y. W.; Cho, Y.; Hong, J.; Jang, A. R.; Chung, H. S.; Hong, W. K.; Jeong, H. Y.; Shin, H. S.; Morris, S. M.; Cha, S.; Sohn, J. I.; Kim, J. M., Thermodynamically Stable Synthesis of Large-Scale and Highly Crystalline Transition Metal Dichalcogenide Monolayers and their Unipolar n–n Heterojunction Devices. *Adv. Mater.* **2017,** *29*, 1702206.

(42) Han, G.; Kybert, N. J.; Naylor, C. H.; Lee, B.; Ping, J.; Park, J.; Kang, J.; Lee, S.; Lee, Y.; Agarwal, R.; Johnson, A. T. C., Seeded Growth of Highly Crystalline Molybdenum Disulphide Monolayers at Controlled Locations. *Nat. Commun.* **2015,** *6*, 6128.

(43) Ribeiro-Soares, J.; Almeida, R. M.; Barros, E. B.; Araujo, P. T.; Dresselhaus, M. S.; Cancado, L. G.; Jorio, A., Group Theory Analysis of Phonons in Two-Dimensional Transition Metal Dichalcogenides. *Phys. Rev. B* **2014,** *90*, 115438.

(44) Zhang, X.; Qiao, X. F.; Shi, W.; Wu, J. B.; Jiang, D. S.; Tan, P. H., Phonon and Raman Scattering of Two-Dimensional Transition Metal Dichalcogenides from Monolayer, Multilayer to Bulk Material. *Chem. Soc. Rev.* **2015,** *44*, 2757-2785.

(45) Chen, Y.; Xi, J.; Dumcenco, D. O.; Liu, Z.; Suenaga, K.; Wang, D.; Shuai, Z.; Huang, Y.-S. S.; Xie, L., Tunable Band Gap Photoluminescence from Atomically Thin Transition-Metal Dichalcogenide Alloys. *ACS Nano* **2013,** *7*, 4610-4616.

(46) Varshni, Y. P., Temperature Dependence of the Energy Gap in Semiconductors. *Physica* **1967,** *34*, 149-154.

(47) Cho, Y.-H.; Gainer, G. H.; Fischer, A. J.; Song, J. J.; Keller, S.; Mishra, U. K.; DenBaars, S. P., "S-shaped" Temperature-Dependent Emission Shift and Carrier Dynamics in InGaN/GaN Multiple Quantum Wells. *Appl. Phys. Lett.* **1998,** *73*, 1370-1372.

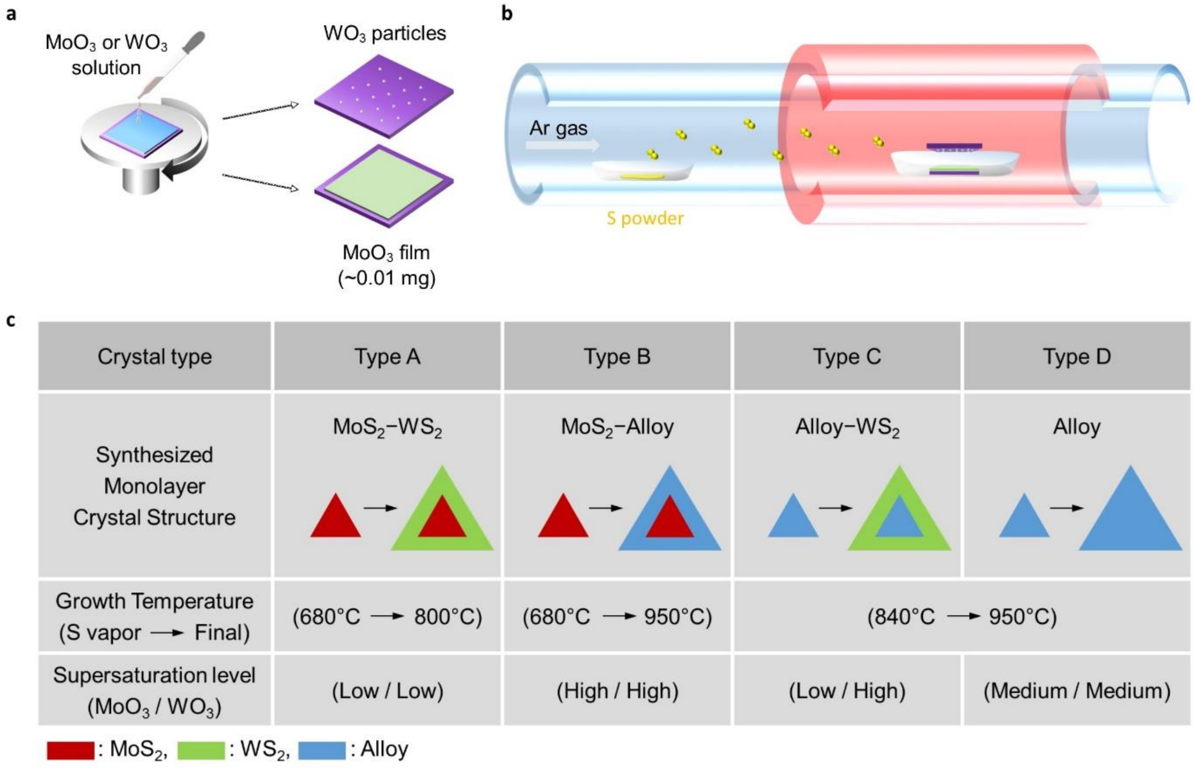

Crystal type	Type A	Type B	Type C	Type D
Synthesized Monolayer Crystal Structure	MoS_2–WS_2	MoS_2–Alloy	Alloy–WS_2	Alloy
Growth Temperature (S vapor → Final)	(680°C → 800°C)	(680°C → 950°C)	(840°C → 950°C)	
Supersaturation level (MoO_3 / WO_3)	(Low / Low)	(High / High)	(Low / High)	(Medium / Medium)

🟥: MoS_2, 🟩: WS_2, 🟦: Alloy

Figure 1. Schematic of the growth process of MoS_2/WS_2 lateral heterostructures and alloys. (a) Solution-processed precursor deposition. The MoO_3 film was deposited by a MoO_3 solution in NH_4OH while the WO_3 particles were scattered by using a WO_3/sodium cholate solution in NH_4OH. (b) Illustration of the synthesis process for the heterostructures and alloys. (c) Condition for each monolayer structure.

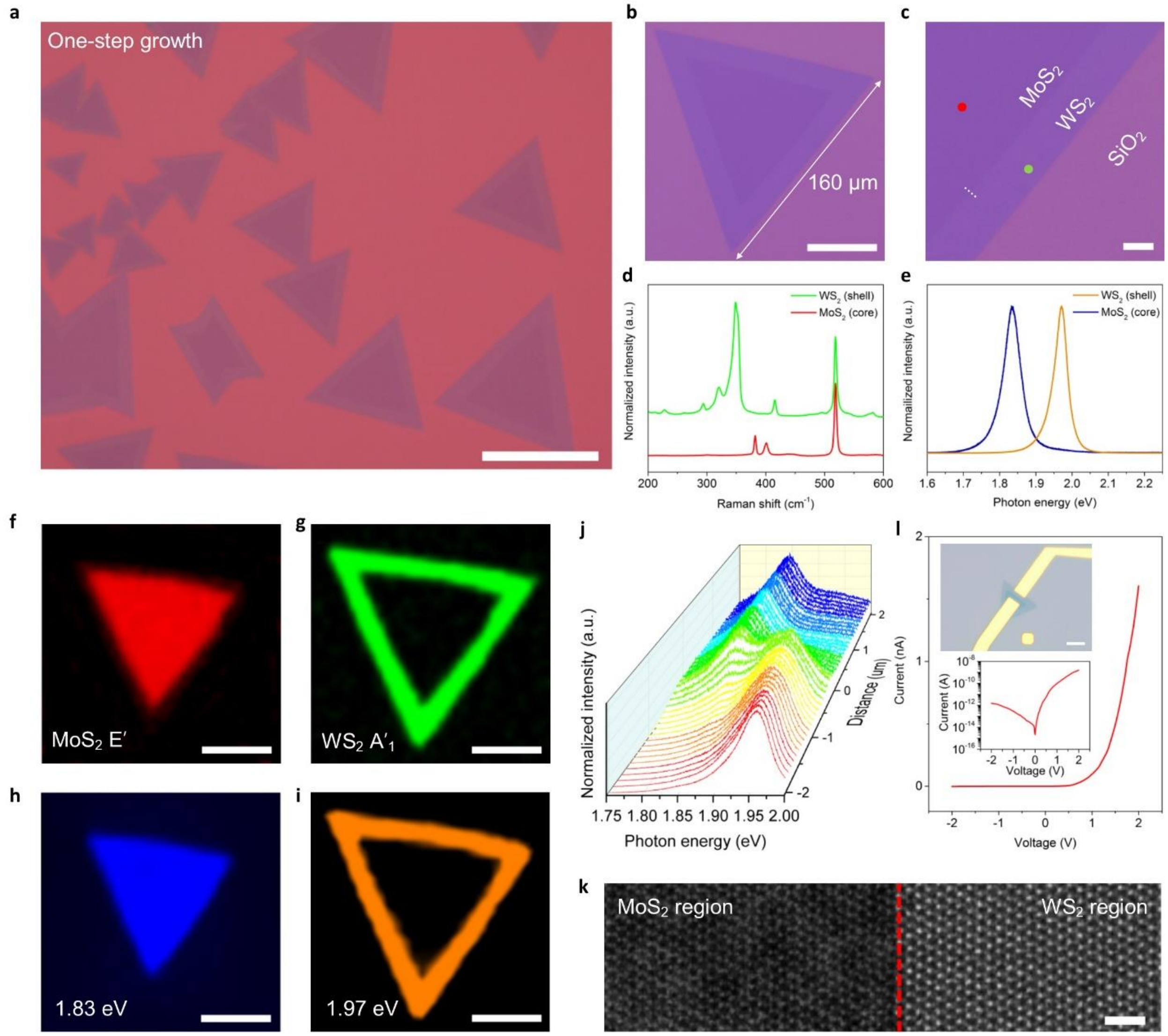

Figure 2. MoS_2/WS_2 heterostructures grown by a one-pot synthesis. (a) Optical image of the MoS_2/WS_2 heterostructure. Scale bar: 100 µm. (b) Optical image of a large-sized MoS_2/WS_2 heterostructure. Scale bar: 50 µm. (c) Enlarged optical image of the interface between the MoS_2 and the WS_2 monolayers. Scale bar: 10 µm. (d-e) Raman and PL spectrum collected from the core and the shell regions. (f-g) Raman mapping images of the E$^{'}$ peak of MoS_2 and the A'$_1$ peak of WS_2. (h-i) PL mapping images of the MoS_2 and the WS_2 emission energy. Scale bar: 50 µm. (j) PL transition at the interface of the heterostructure marked with white dots in (c). (k) STEM image

of the interface of the heterostructure. Scale bar: 1 nm. (l) Linear I-V curve, optical image (top inset) and log scale I-V curve (bottom inset) of the MoS_2/WS_2 heterostructured device.

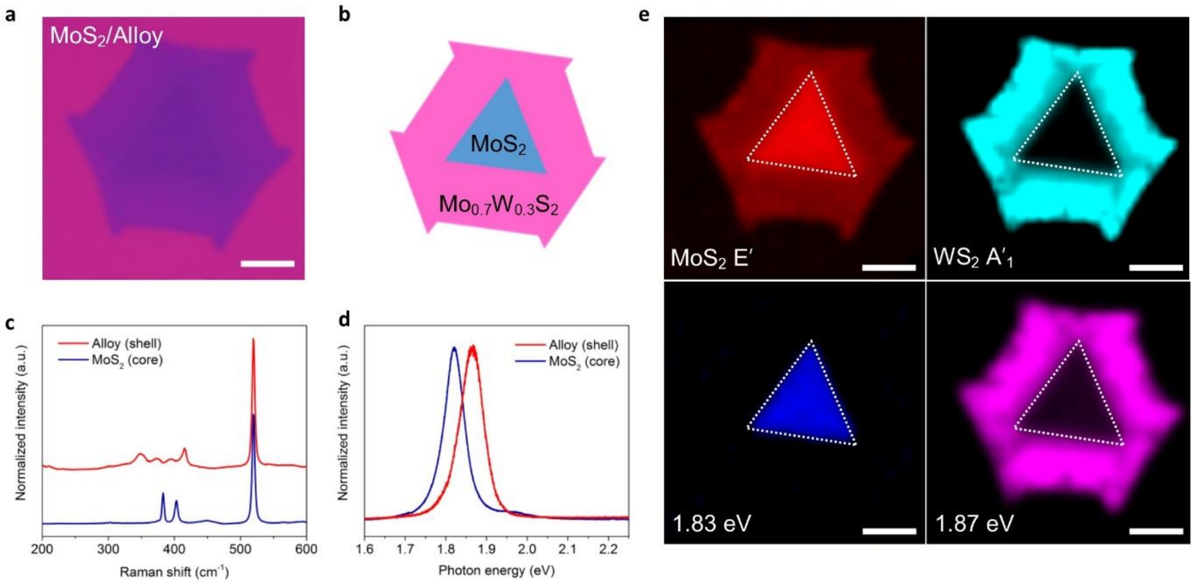

Figure 3. MoS_2/Alloy heterostructures. (a) Optical image of the MoS_2/Alloy heterostructure monolayer. The contrast of the image was adjusted to show the core and the outer region clearly. (b) Schematic of the synthesized MoS_2/Alloy heterostructure monolayer. (c-d) Raman and PL spectrum collected from the core and the shell layers. (e) Raman and PL mapping images. All scale bars: 20 µm.

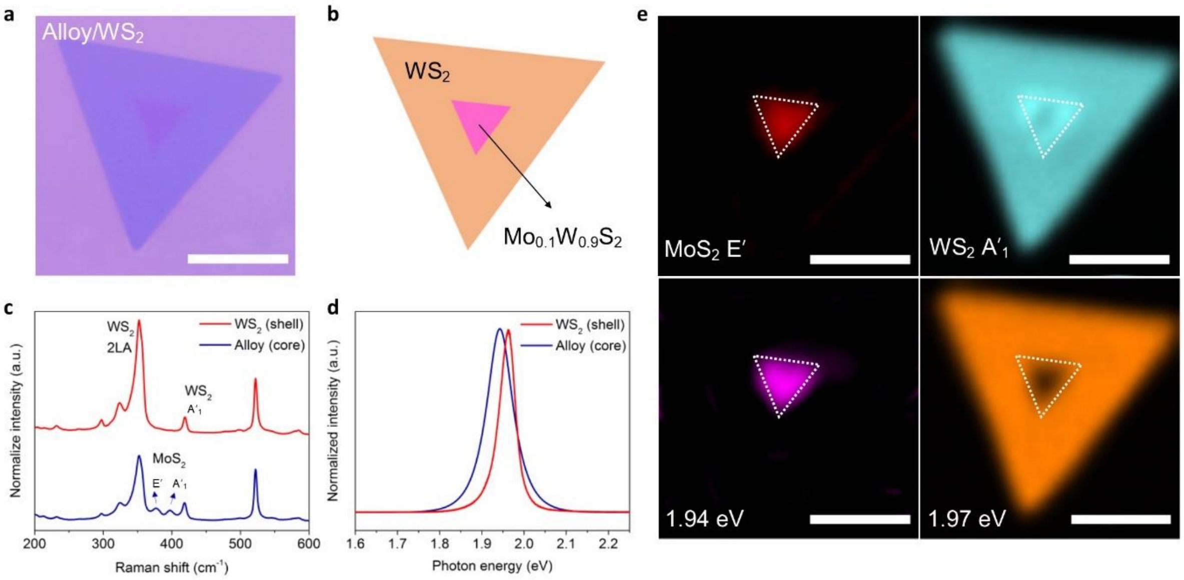

Figure 4. Alloy/WS$_2$ heterostructures. (a) Optical image of the Alloy/WS$_2$ heterostructure monolayer. The contrast of the image was adjusted to show the core and the outer region clearly. (b) Schematic of the synthesized Alloy/WS$_2$ heterostructure monolayer. (c-d) Raman and PL spectrum collected from the core and the shell layers. (e) Raman and PL mapping images. All scale bars: 50 μm.

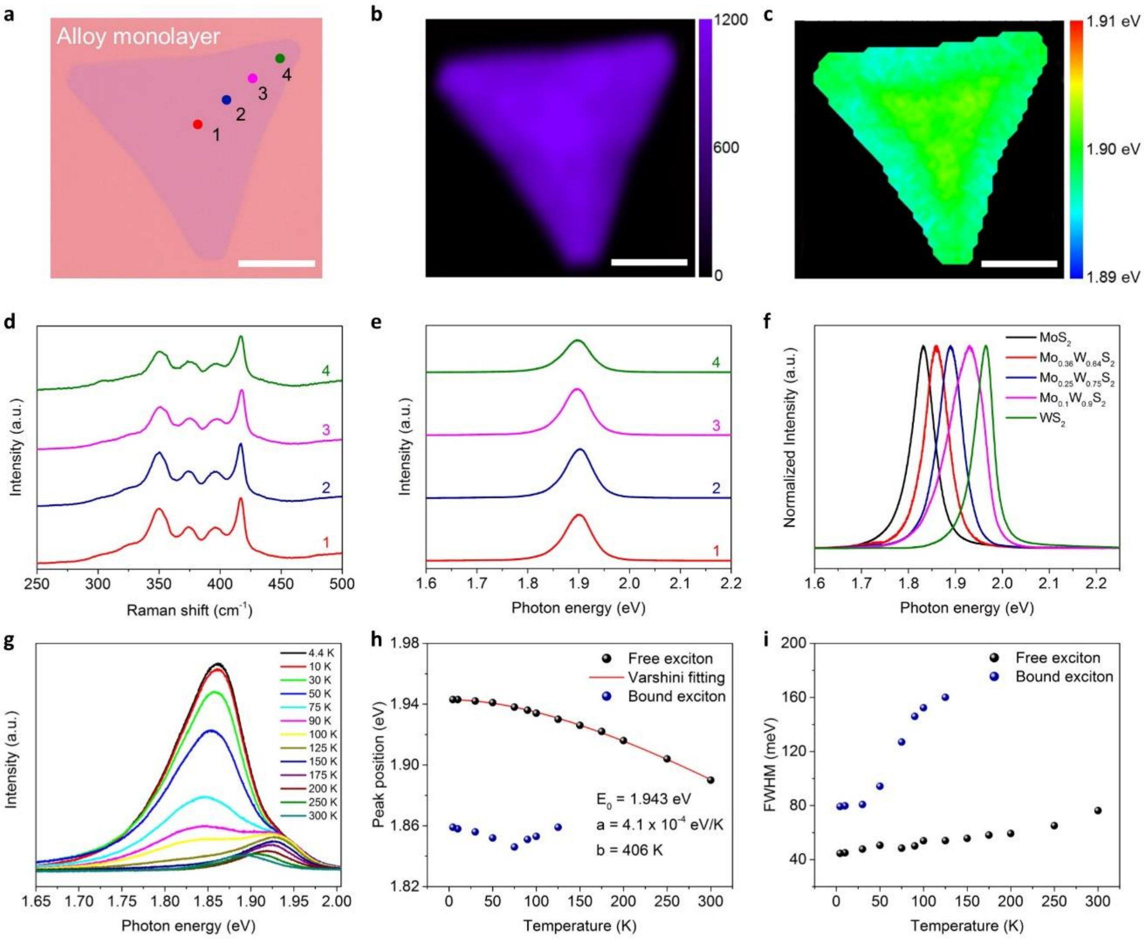

Figure 5. $Mo_{1-x}W_xS_2$ Alloy monolayers. (a) Optical image of the $Mo_{1-x}W_xS_2$ alloy monolayer. (b) PL intensity mapping image at 1.90 eV. (c) PL position mapping image. All scale bars: 20 μm. (d-e) Raman and PL spectrum collected from the marked points in (a). (f) PL spectrum of the composition ratio-controlled alloy monolayers. (g) Temperature-dependent PL spectrum of the alloy monolayer. (h) Peak position of the free excitons and the bound excitons as a function of temperature. (i) FWHM of the free excitons and the bound excitons as a function of temperature.

Table of Contents